AIP | Journal of Applied Physics

Minimum quench power dissipation and current non-uniformity in international thermonuclear experimental reactor type NbTi cable-in-conduit conductor samples under direct current conditions

G. Rolando, E. P. A. van Lanen, and A. Nijhuis

Citation: J. Appl. Phys. **111**, 093904 (2012); doi: 10.1063/1.4709438
View online: http://dx.doi.org/10.1063/1.4709438
View Table of Contents: http://jap.aip.org/resource/1/JAPIAU/v111/i9
Published by the American Institute of Physics.

Minimum quench power dissipation and current non-uniformity in international thermonuclear experimental reactor type NbTi cable-in-conduit conductor samples under direct current conditions

G. Rolando, E. P. A. van Lanen, and A. Nijhuis
Energy, Materials and Systems, Faculty of Science and Technology, University of Twente, P.O. Box 217, 7500 AE Enschede, The Netherlands

(Received 13 October 2011; accepted 26 March 2012; published online 2 May 2012)

The level of current non-uniformity in NbTi cable-in-conduit conductors (CICCs) sections near the joints in combination with the magnetic field profile needs attention in view of proper joint design. The strand joule power and current distribution at quench under DC conditions of two samples of ITER poloidal field coil conductors, as tested in the SULTAN facility, and of the so called PFCI model coil insert, have been analyzed with the numerical cable model JackPot. The precise trajectories of all individual strands, joint design, cabling configuration, spatial distribution of the magnetic field, sample geometry, and experimentally determined interstrand resistance distributions have been taken into account. Although unable to predict the quench point due to the lack of a thermal-hydraulic routine, the model allows to assess the instantaneous strand power at quench and its local distribution in the cable once the quench conditions in terms of current and temperature are experimentally known. The analysis points out the relation of the above mentioned factors with the DC quench stability of both short samples and coils. The possible small scale and local electrical-thermal interactions were ignored in order to examine the relevance of such effects in the overall prediction of the CICC performance. The electromagnetic code shows an excellent quantitative predictive potential for CICC transport properties, excluding any freedom for matching the results. The influence of the local thermal effects in the modeling is identified as being marginal and far less than the generally accepted temperature margin for safe operation. © *2012 American Institute of Physics*. [http://dx.doi.org/10.1063/1.4709438]

I. INTRODUCTION

Cable-in-conduit conductors (CICCs) are commonly used in fusion magnets due to their elevated stability and current carrying potential. The CICCs foreseen for the poloidal field (PF) coils of the fusion reactor ITER will contain hundreds of NbTi strands twisted and compacted together in multiple cabling stages, see Table I. High currents require large cable diameters and produce a significant self field that, summed to the background one, determines the magnetic field distribution over the CICC cross section. Following their trajectories from one side of the conductor to the opposite, the twisted strands experience large variations of the local magnetic field and may reach elevated electric field levels on extremely localised sections. As a result, the power dissipation over the cross section is not homogeneous. On top of that, the currents in the strands of CICCs may not be uniformly distributed. Typical sources of unbalance are the joints at the extremities of a conductor. The spread in the electrical resistances between superconducting strands and the normal conducting parts in the terminals of the current leads causes a corresponding spread in the currents of the strands. The combination of magnet self-field and current non-uniformity results in local hot spots that can lead, in the worst case, to premature quenches.

The aim of this work is to explore quantitatively the quench limitations of ITER type NbTi CICC in relation to the joint layout and magnetic field map. From the analysis, the main parameters affecting the current unbalance inside a CICC are also identified in view of the optimisation of the joint design for magnets.

To assess the performance of the full size PF conductor, both short samples and a superconducting insert coil have been manufactured. The poloidal field insert sample (PFIS) was tested in the SULTAN facility at CRPP (Switzerland) in 2004. The DC behaviour of the sample revealed low performance compared to design expectations due to early quench of the conductor.[1] The cause of this result was attributed to current unbalance introduced by the joints that could not be redistributed before the high field region of the sample. As a result, the overloaded strands reached saturation, which eventually led to a quench of the entire conductor.[2,3] An important role in the phenomenon was recognized to be played by the cable self field, producing a considerable magnetic field gradient over the conductor cross section.[4,5]

In order to get a better understanding of the behaviour of high current NbTi CICCs and joints in relevant ITER operational conditions, the poloidal field conductor insert (PFCI) was built in Europe and tested at JAERI Naka (Japan) in 2008. Although it was constructed using the same cable as the PFIS, the PFCI DC behaviour met the ITER operation requirements without the premature quenches observed in the SULTAN sample. The improved performance was attributed to the longer conductor length and increased distance between the joints and the high field region.[6] More recently, the first Chinese PF conductor sample (PFCN1) was tested successfully at the SULTAN facility. The sample featured a

TABLE I. Design and operating parameters of ITER PF coils.

	PF2,3,4	PF5	PF1,6
Type of strand	NbTi	NbTi	NbTi
Number of superconducting strands	720	1152	1440
Number of Cu strands	360	6	–
Nominal operating current [kA]	50.0	52.0	48.0
Nominal effective peak field [T] (external + self field)	5.0	5.7	6.4
Operating temperature [K]	4.5	4.5	4.5

new layout for the upper terminations together with a "U" bend bottom to avoid the current unbalance produced by conventional joints.

II. CONDUCTOR AND SAMPLE LAYOUT

A. PFIS details

The preparation and instrumentation details of the PFIS can be found in Ref. 7. The sample comprises two conductor sections ("legs") connected at one end by a hairpin joint, see Fig. 1 left. One section consists of the regular CICC of the poloidal field coil insert (W), while the second had the steel wraps around the final stage sub-cables completely removed (NW). The PFIS size is the standard one for SULTAN samples, about 3.5 m long, including the bottom joint and the upper connections. The main parameters for the two legs are summarized in Table IV (Refs. 7 and 8) in Appendix.

B. PFCI details

The design and manufacture of the PFCI are described in Refs. 9–11. The PFCI is a single-layer solenoid wound out of 50 m of the same NbTi CICC used for the PFIS W (see Fig. 1 right), see Table V in Appendix. The upper section of the main winding was connected to an intermediate joint to test the joint behaviour in ITER-relevant magnetic field conditions.

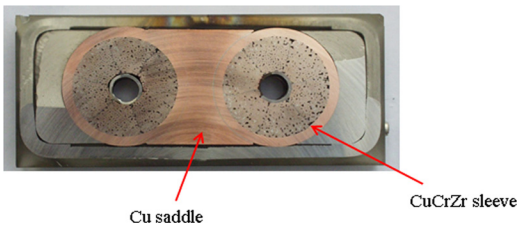

FIG. 2. PFIS bottom joint cross section.

C. PFCN1 details

Unlikely the PFIS and PFCI samples, the PFCN1 constitutes an example of PF2 conductor, see Table I. Details about its assembly are reported in Ref. 12; while the main parameters of the conductor can be found in Table VI in Appendix. The PFCN1 was tested in the SULTAN facility; therefore, it features the same structure of the PFIS sample. However, major differences exist in the layout of the terminations and bottom joint of the two samples as detailed in Sec. II D.

D. Differences and similarities in the joint/termination of the samples

The terminations of the PFIS were prepared by swaging the cable into CuCrZr sleeves, see Fig. 2. The bonding between cable and sleeve was obtained by removing the Ni coating from the strands at the cable surface and replacing it with Ag coating. In addition, the inner surface of the sleeve was tinned. At the bottom joint, the sleeves were joined by five copper saddles, while copper plates connected the upper terminations to the secondary winding of the SULTAN transformer. The main parameters for the joints are summarized in Table IV (Refs. 7 and 8) in Appendix.

The PFCI sample featured the same joint/terminations design of the PFIS. However, improvements were made to the residual-resistance ratio (RRR) of the materials and the strand-sleeve soldering technique as detailed in Table V in Appendix.

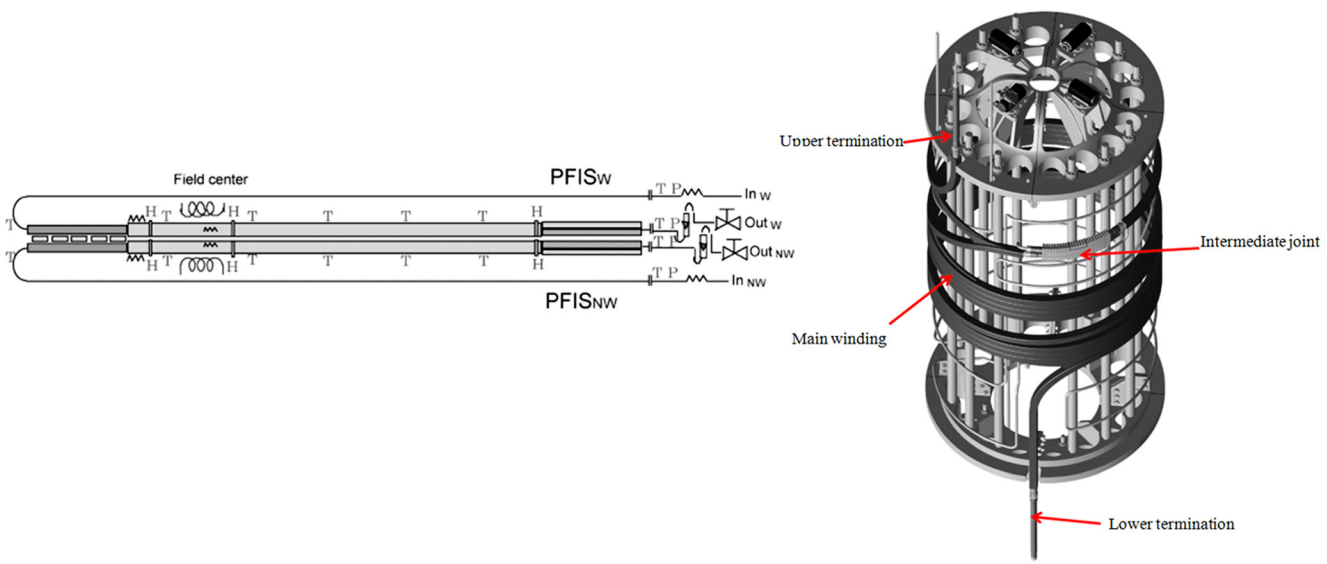

FIG. 1. PFIS (left) and PFCI (right) samples layout.[1,10]

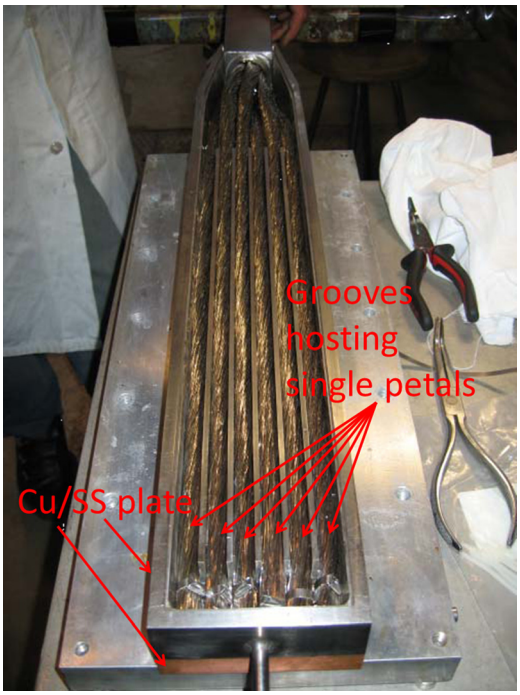

FIG. 3. PFCN1 upper termination featuring the combo box design.[13]

The most important innovations of the PFCN1 are represented by the new layouts of both upper terminations and bottom joint. For the connections to the SULTAN transformer, a combo box solution developed at Commissariat a l'Energie Atomique (CEA) was adopted. As shown in Fig. 3, wraps are removed at the extremities of the cable, which allows petals to be individually soldered into grooves machined in a copper/stainless steel plate. The bottom joint was replaced by a "U" bend inserted into a hairpin bending box, see Fig. 4.

III. JACKPOT CODE

In this study, the strand behaviour at quench under DC conditions of the conductors has been analysed with the code JackPot. JackPot models the CICC as a network of superconducting and resistive elements as shown in Fig. 5. The strong point of the code consists in its ability to follow the precise trajectories of all the strands inside a CICC. Therefore, all the required quantities are calculated directly from either the geometry of the strands or experimental measurements and no free parameters are present in the model.

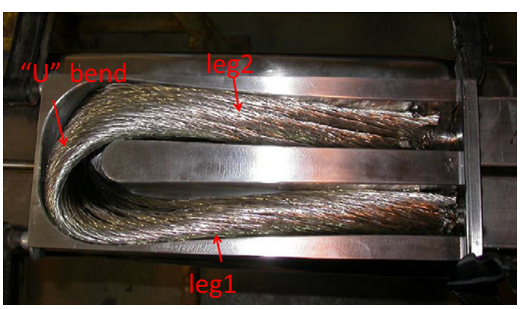

FIG. 4. PFCN1 bottom "U" bend in the hairpin box.

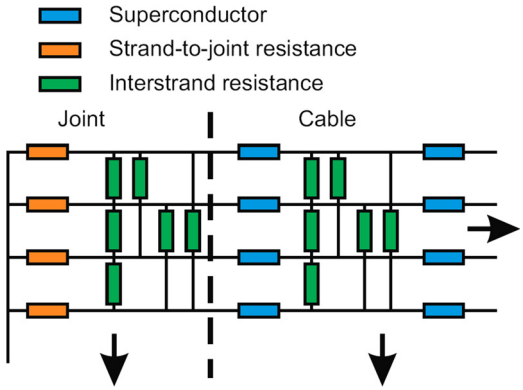

FIG. 5. Electrical network modelling the CICC in the code JackPot.

The code divides the cable along its length in a number of sections where the distributed contact between strands or between strands and joint is simulated by a single conductance. The value of the resistors is the ratio of a resistivity parameter ρ, accounting for the material properties of the system, and the contact area A, calculated from the strand trajectories

$$R = \frac{\rho}{A}. \tag{1}$$

The resistivity parameter ρ used in the model, see Eq. (1), expressed in units of $\Omega{\cdot}m^2$, corresponds to the product of the "classic" resistivity and the length of the resistor. Being related to the materials, different resistivity parameters are expected for the interstrand and strand-to-joint resistances. The values of the interstrand (ρss) and strand-to-joint (ρsj) resistivity parameters used in the analysis are summarized in Table II.

The electrical behaviour of the superconducting strands is modeled according to the conventional power law

$$V = V_C\left(\frac{I}{I_C}\right)^n, \tag{2}$$

where $V_C = 10\,\mu V/m$ and I_c is the critical current of the strands.[14,15]

For NbTi strands, the scaling law requires two parameters, namely, the temperature and the magnetic field. In the model, the temperature is a constant input parameter. On the contrary, the local magnetic field is evaluated at every strand

TABLE II. Summary of the JackPot model parameters used in the PFIS simulation.

	PFIS W	PFIS NW
Interstrand resistivity parameter—cable region [$\times 10^{-12}\,\Omega\,m^2$]	159	101
Interstrand resistivity parameter—joint region [$\times 10^{-12}\,\Omega\,m^2$]	122	42
Strand-to-joint resistivity parameter—joint region [$\times 10^{-12}\,\Omega\,m^2$]	2100	97
Solder layer thickness [m]	0	0

section as the sum of the background and self-field from the Biot-Savart law, see Fig. 13. At each strand section Kirchoff's equations are solved with the MATLAB™ built in nonlinear solver *fsolve*. More details about the code can be found in Refs. 16 and 17.

Being a DC electromagnetic model, without a thermal-hydraulic description of the conductor, JackPot cannot be used to predict the quench point of a CICC or describe the quench characteristics (i.e., occurrence of sudden transitions). However, given the temperature and current conditions characterizing the quench, which are known from the experiment, the code does accurately calculate the voltages and currents in the cable. The precise trajectories of all individual strands, joint design, cabling configuration, spatial distribution of the magnetic field, sample geometry, and experimentally determined interstrand resistance distributions are taken into account. Therefore, the code allows for the determination of the power dissipation at the instant at which the sample quenched during the experiment. These values set a conservative limit to the allowable heat generation at quench, since the code assumes a uniform temperature distribution in the cross-section. In reality, quenches appear in the form of extremely localized hot spots with likely higher temperature than the average cable measured one. However, we assume that the local thermal-electrical interactions have a minor effect on the overall analysis. To which extent this assumption is justified will follow implicitly from the analysis results.

IV. MODELLING OF THE ANALYSED SAMPLES

Before proceeding to the simulation results, some modeling details are discussed, which are relevant to the DC stability of the analyzed samples.

A. Finite element model modeling of joint and terminations

To reproduce the current unbalance inside the sample the code has been upgraded with the coupling with a finite element model (FEM) of the joints realized in COMSOL™, see Fig. 6.

B. Model parameters

The current distribution among the strand is determined by the interstrand and strand to joint contacts. Table II summarises the parameters for the PFIS simulation. The parameters ρss and ρsj are fixed by matching the results from simulations with interstrand[18] and joint[19] resistance measurements.

The parameter set of PFIS W has also been used in the simulations of PFCI and PFCN1 since no specific interstrand resistance measurements exist for these conductors. Moreover, similar resistivity values are expected, being determined only by the choice of the materials.

As shown in Table II, the addition of solder in the joints to improve the electrical contact between strands and sleeve is included in the model. Similarly, the presence of wraps around the last cabling stage bundles, which prevents current re-distribution,[18] is also taken into account. The complete DC current model for joints has been validated through measurements.[20]

In the PFIS, although the use of solder is reported, its thickness has been neglected in the simulation due to the experimentally observed poor bonding.[9]

Following the adoption of a different soldering technique in the PFCI, it is likely that a non-zero solder layer is present in the joints of the sample. However, no information is available regarding its possible thickness. On this account, the solder layer is assumed negligible in the calculations, after having verified that it would not produce in any case significant effects on the final result.

C. Conductor temperature

A general assumption in the code is the temperature being uniform everywhere in the CICC, both in the cross section and along the axial length. Although being acceptable for short samples such as SULTAN ones, where the high field region has a total length of about 0.5 m, this approximation is not adequate for long coils such as the PFCI. The issue is of particular relevance for NbTi CICCs, due to their strong critical current dependence on temperature. Moreover, the PFCI test configuration featured a double cooling circuit.

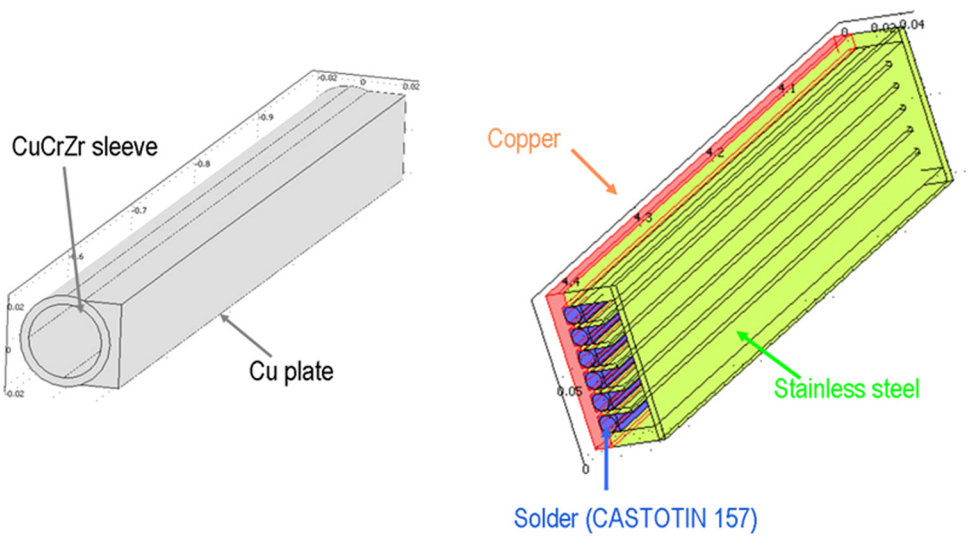

FIG. 6. Finite element models of the PFIS/PFCI (left) and the PFCN1 (right) terminations.

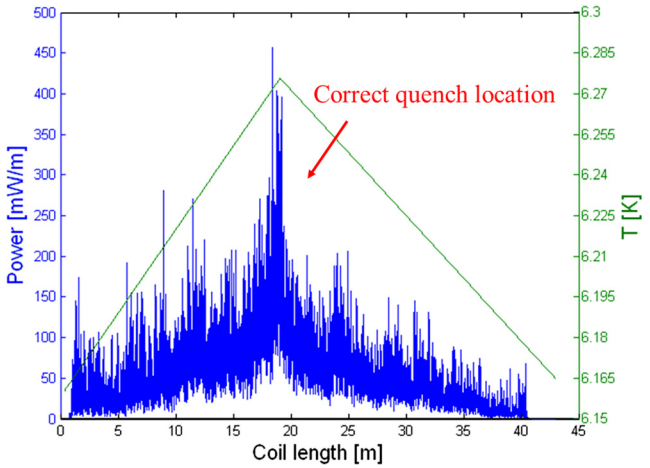

FIG. 7. PFCI Run # 035-01 power dissipation distribution at quench taking into account the coil axial temperature profile (Y secondary axis).

This generally resulted in a slightly lower temperature in the conductor section close to the intermediate joint compared to the middle of the main winding. Therefore, a longitudinal temperature profile has been implemented in the PFCI simulations through a linear interpolation of the temperature measurements at inlet, outlet, and middle of the main winding. As an example, assuming a uniform longitudinal temperature would lead in the case of Run # 035-01 (a current sharing temperature test with a transport current of 55 kA and peak background field of 6 T) to an unrealistically huge dissipation close to the intermediate joint due to the combination of current unbalance and magnetic field. Using the best available approximation of the axial temperature gradient sets the peak dissipation to its correct location close to the middle of the coil, where it was experimentally recorded, see Fig. 7.

V. VALIDATION OF SIMULATION RESULTS

The simulations have been validated through the comparison with measurements for both critical current (Ic) and current sharing temperature (Tcs) runs.

Fig. 8 shows a summary of measured and calculated critical currents for different background fields for the two legs of PFIS. The agreement between simulation and experiment is found to be within 0.12 K and few kA for Tcs and Ic runs, respectively.

Due to the observed tendency of PFCN1 to quench even at relatively low currents without appreciable transition, critical current and current sharing temperature could be measured only for few experimental runs. Therefore, it was not possible to draw an analogous graph for this conductor. However, even for PFCN1 the code is able to properly describe the behaviour of the sample. This is illustrated in Fig. 9 where the simulated and measured evolutions of the electric field during a Tcs run are compared.

In Figs. 8 and 9, the similarity between the slopes of the simulated and experimental curves should be noticed. Similar slopes indicate that the current unbalance of the sample could be reproduced by the code thanks to the detailed modelling of cable and joints.

The comparison between simulation and measurement appears to be somewhat less precise for the PFCI. In particular, the simulation is found to generally shift the instant of quench. In Tcs runs, the temperature at which the coil reaches the quench electric field is on average 80 mK higher in the simulation than in the measurements. In spite of this, the PFCI simulation results are much better than the predictions presented in Refs. 21–23, where the deviation between prediction and experiment amounts up to more than 0.4 K. The origin of the shift is currently object of further investigations.

VI. DISSIPATION SPOT LENGTH

The power generation inside a CICC at the beginning of a quench is in the form of local dissipation spots along the strands. The length of a dissipation spot depends on the properties of the strand (n-value, Ic(B) steepness) and cable (twist pitch, void fraction, diameter). The extension of the dissipation spot is found by plotting the strand peak power density versus cable quench current for different normalization volumes (i.e., dissipation lengths), see Fig. 10, as explained below.

To compare the performance of samples made of different strands, the power dissipation is normalized to a strand volume. The strand is cut into sections along its length and

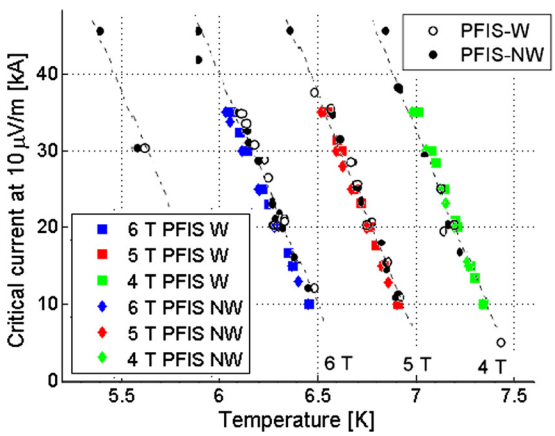

FIG. 8. Summary of the simulated (square and diamond) and measured (dot) Ic and Tcs for PFIS.

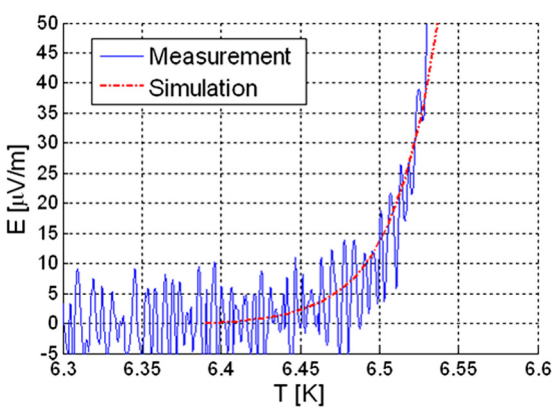

FIG. 9. Electric field evolution versus temperature for PFCN1 Tcs Run #SSPF2D180510 with transport current 20 kA and SULTAN background field 5 T.

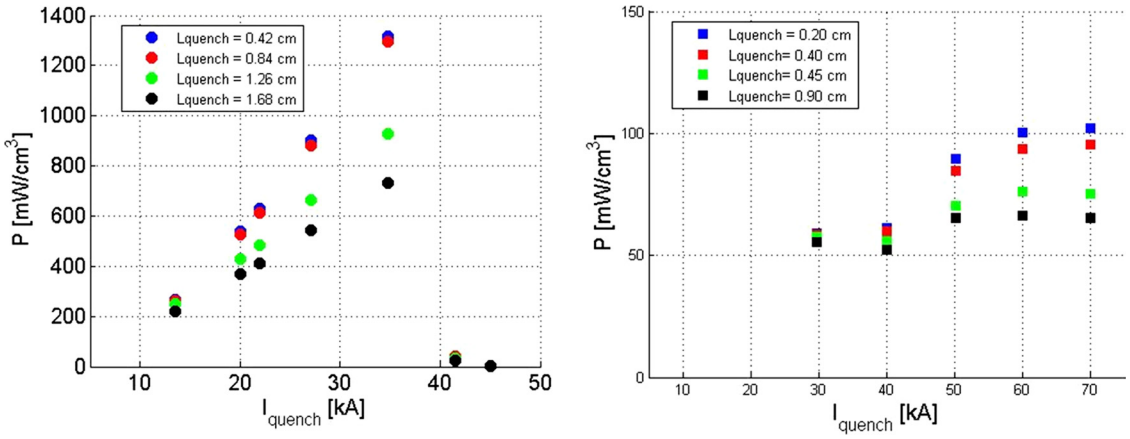

FIG. 10. Strand dissipation versus quench current for different quench lengths of the PFIS (left) and PFCN1 (right).

for each of them the local power dissipation density is calculated. The power density computation has been repeated for strand sections of increasing lengths, see legends of plots in Fig. 10. For section lengths shorter or equal than the dissipation spot, the power density will have a constant value. When the strand section length exceeds the dissipation spot, the power density will drastically drop since the Joule dissipation outside the quench spot is minimal. Using the PFIS case as an example, when the strands are cut into sections of length 0.42 and 0.84 cm, the same power dissipation density is obtained. However, when the section length is further increased to 1.26 cm, the power dissipation density significantly reduces.

Since they are wound out of the same cable, the dissipation spot lengths of PFIS and PFCI are found, not surprisingly, to coincide (~8.4 mm). The dissipation spot length of the PFCN1 is instead lower (~4.0 mm), which is likely to be connected to the sharper V-I transition of its strands[14] and the different conductor geometry.

VII. QUENCH POWER DISTRIBUTION

Following the precise trajectories of all the single strands inside a CICC, JackPot is the first and only available code at present to allow the visualization and quantification of the dissipation spots inside a sample. Figs. 11 and 12 show the power dissipation at quench for the strands of PFIS W in the cross section where the strand peak power density is located. It can be observed that while only few strands show significant dissipation at 41.5 kA, the power generation is spread over a wider part of the cross section at low currents. An analogous behaviour is observed for the other analyzed samples. Since, as shown in the next section, there is no significant variation of the current unbalance with quench current for the PFCI and PFCN1, an increased current non-uniformity cannot be the cause of the varying dissipation distributions. Therefore, the difference is likely to arise from the steeper magnetic field gradient at high currents due to the increasing weight of the self-field of the conductor.

The importance of the self-field in determining the location of quench can also be seen in the fact that in both cases the highest power dissipation takes place at the inner edge of the conductor. At this position, the peak field resulting from the sum of background and self-field is located. The self-field of the PFIS and the background field profile of the SULTAN facility are plotted in Fig. 13.

The axial strand power distribution for the same runs of PFIS W is illustrated in Figs. 14 and 15. Also in this

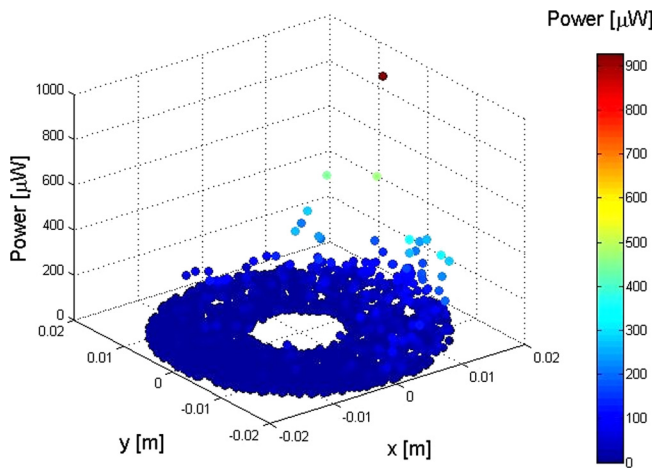

FIG. 11. Strand dissipation distribution at quench in the cross section of PFIS W where the strand peak power generation is located for 13.5 kA at 6 T background field.

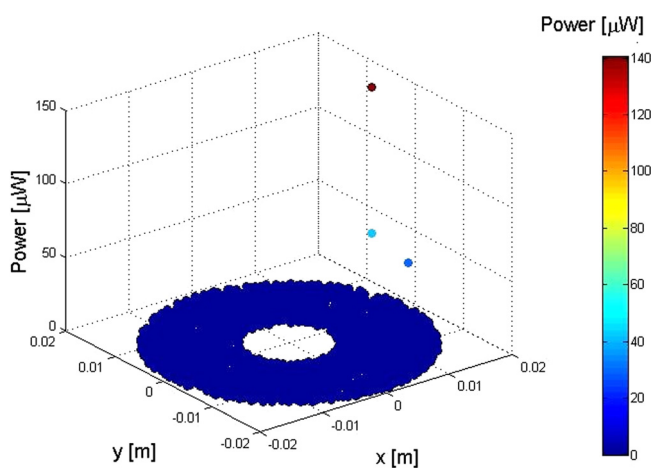

FIG. 12. Strand dissipation distribution at quench in the cross section of PFIS W where the strand peak power generation is located for 41.5 kA at 6 T background field.

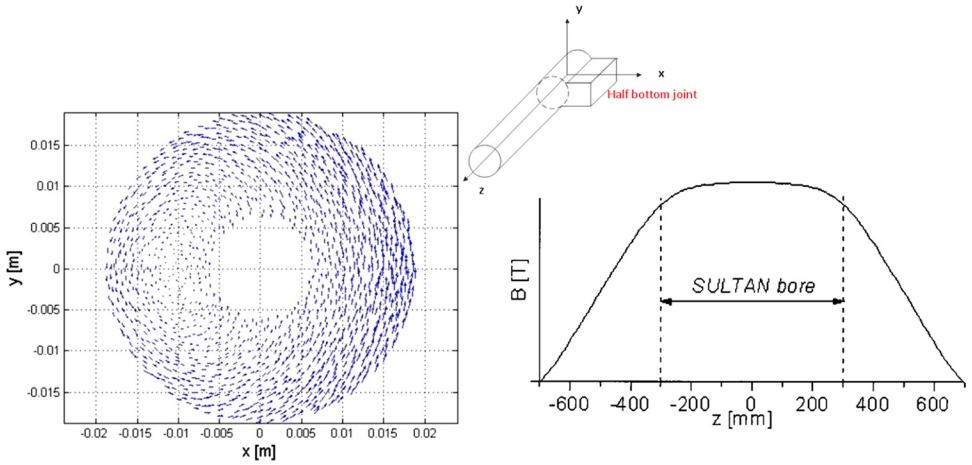

FIG. 13. Vector plot of the self-field over the cross section of a PFIS leg (left) and SULTAN background field axial profile (right). The self-field in the centre of the CICC is not zero due to the second leg of the U-shaped sample carrying an opposing current. The self-field is higher at the surface of cable due to the assumption of uniform current distribution over the cross section. At the inner edge ($x \sim 18$ mm) self and background field sum, while they subtract at the outer edge ($x \sim -18$ mm).The insert shows one leg of the PFIS sample with the used system of reference.

direction, the number of strands taking part in the power generation at quench reduces with increasing transport current. Similar behaviours are observed for the other analyzed samples.

In Figs. 14 and 15, the effect of the joint layout on the current distribution among the strands, and therefore, on the power dissipation distribution can also be observed. The high field region of SULTAN extends approximately between -0.2 m and 0.2 m in the z direction and features an almost uniform magnetic field. However, the resulting strand axial dissipation distribution is not symmetric to the high field region centre, as it would be expected in the case of uniform current distribution. The observed asymmetry is a consequence of the combination of joint design, wraps, self-field, and twist pitch. The total strand power distribution along the PFIS is illustrated for both legs of the sample in the same operating conditions in Fig. 16. The power distribution resulting from a hypothetical rotation of 180° of the copper plates in both terminations of PFIS W is also included to show the effect of the joint layout on the power distribution. In the PFIS W the limited contact angle sleeve-Cu plate, its length and position with respect to peak field of the conductor combined with the twist pitch sequence produce a current unbalance that can be hardly redistributed due to the presence of wraps. The configuration is such that the overloaded strands enter the high field region between $z = 0$ and $z = 0.1$ m causing an asymmetric dissipation distribution. Removing the wraps in the joint proves to be effective in reducing the current unbalance. In fact the power dissipation of PFIS NW is more symmetric than that of PFIS W. The rotation of the connection plates at the extremities of the sample leg is also found to help in achieving a more uniform power spread. This demonstrates the importance of the joint design on the conductor performance, especially for short samples as the ones tested in SULTAN.

Being JackPot, a pure electromagnetic model and not including a thermo-hydraulic description of the CICC, it cannot be used to predict quenches. However, when the experimental quench point is known in terms of quench current, temperature, or electric field, the instantaneous power dissipation can be computed. The power densities generated in the three samples in the entire cable and in the strand with the peak dissipation are illustrated in Figs. 17 and 18. In the analysis, the quench point has been defined in terms of the experimentally measured temperature or electric field at take-off. An error has also been taken into account corresponding to the uncertainty on the take-off instant.

The points in Figs. 17 and 18 have been obtained from simulations at different magnetic fields and temperatures along the entire current range explored during the experimental tests. From the plots a correlation among the

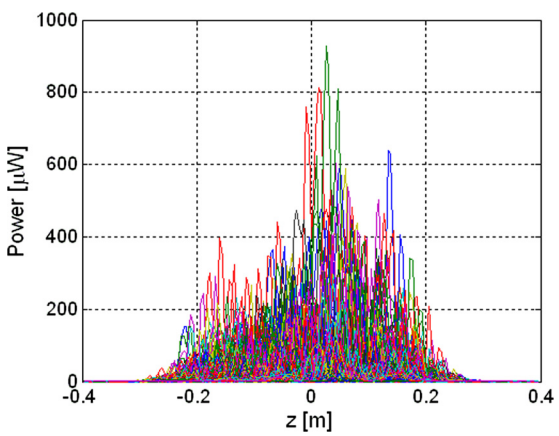

FIG. 14. Strand dissipation distribution along the z-axis of PFIS W for 13.5 kA at 6 T background field.

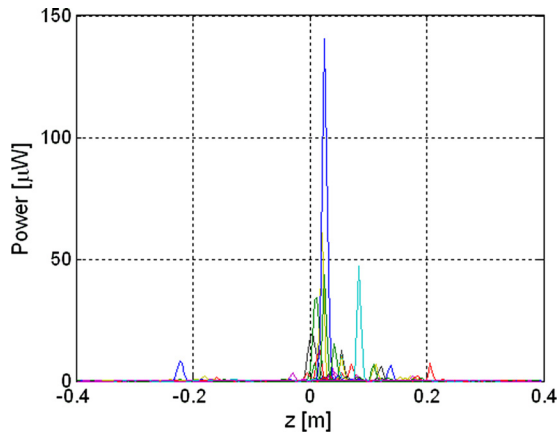

FIG. 15. Strand dissipation distribution along the z-axis of PFIS W for 41.5 kA at 6 T background field.

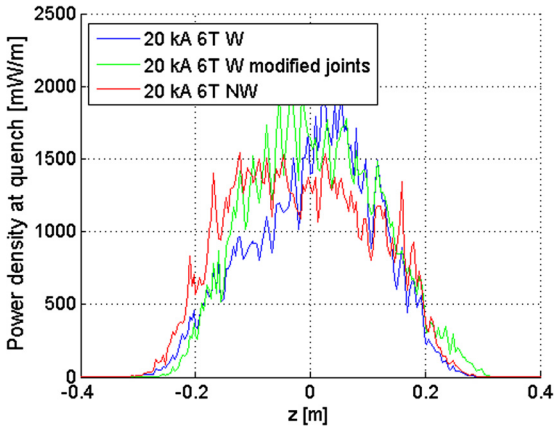

FIG. 16. Strand power dissipation distribution along PFIS z-axis.

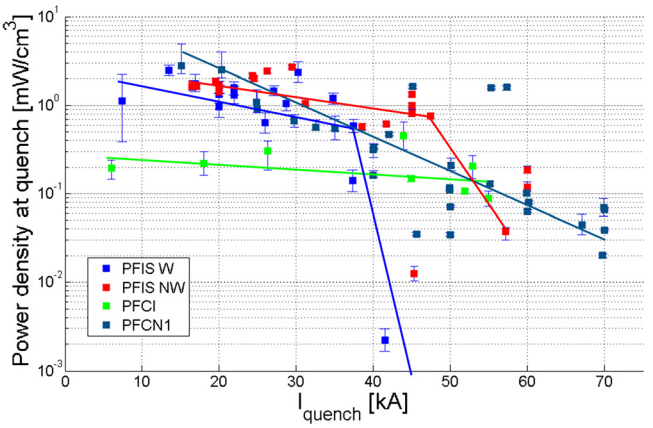

FIG. 18. Cable power dissipation density at quench. Solid lines show the sample trend.

simulations of each sample can be observed, which has been represented through solid lines.

In the PFIS, both cable and strand peak power dissipation densities evolve in a similar way, dropping at 35–40 kA for the leg with wraps, while a stable behaviour is maintained in the leg without wraps up to higher currents (~45 kA). These current levels correspond to the experimentally observed thresholds for sudden quenches in the samples.[1] The knee in the strand power dissipation at quench of the PFIS is interpreted in terms of different quench regimes (cable and strand stability) at low and high currents as already reported for Rutherford and triplex cables as well as CICCs.[24–26] In triplex cables, increasing current non-uniformity has also been associated to a reduced current threshold for quench regime transition. The same behaviour is also seen in the PFIS where, in the left leg, the presence of wraps highly impedes current redistribution, therefore, causing an earlier transition to the strand quench behaviour. The scarcity of measurements above the knee combined with the adoption of changing test conditions (ramp rate and He flow rate) for a significant number of test points make it not possible to draw further conclusions from the available data. As additional remark, the idea that the knee may result from an underestimation of the quenching average cable/strand temperature, increasing with cable current, seems implausible. There are no arguments to support the sudden appearance of such a strong temperature measurement error. Only a change in quench regime (transition to strand quench regime) would be likely to produce a sharper increase of the quenching strand temperature, but this would also be associated to a reduced quench power. Moreover, it would not solve the knee in the cable power dissipation density, for which the measured average strand temperature is the only available practical and valid value.

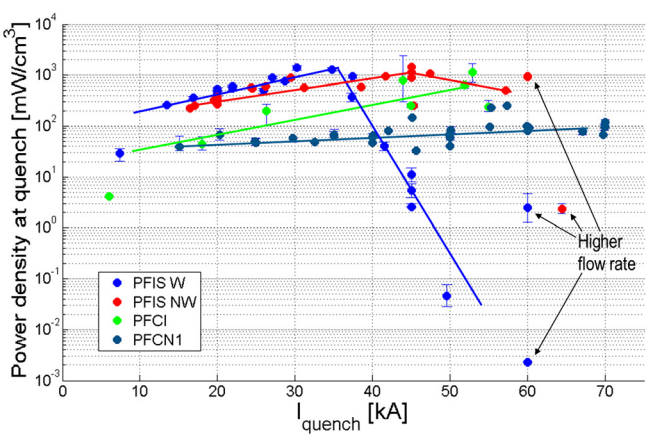

FIG. 17. Strand peak power dissipation density at quench. Solid lines show the sample trend.

The cable and strand peak power dissipation of the PFCI follow trends analogous to what observed for the PFIS in the cable quench regime. The one order of magnitude difference in the strand peak power density of this sample indicates better current redistribution. The lower cable dissipation is, instead, to be attributed to the different B-field gradient of the PFCI in combination with the temperature gradient along the winding. No clear sign of quench regime transition could be found for the PFCI, possibly because it lies beyond the tested experimental range.

The cable power dissipation of the PFCN1 is higher than that of the PFCI, but in the same range of the PFIS one since the two samples feature similar magnetic field and temperature gradients in their high field regions. However, the strand peak power dissipation at quench is much lower due to a better current distribution among the strands. Furthermore, unlike the PFIS samples and PFCI, it remains quite constant in the whole tested range.

An interesting observation is that the PFIS cables could actually reach higher local peak power densities than the PFCN1 and to a less extent than the PFCI. A correlation with the level of current non-uniformity seems credible and is discussed in Sec. VIII.

VIII. CURRENT UNBALANCE

The claim that current unbalance is the main driver for the early quenches in the PFIS cable is justified with Fig. 19. The plot shows the ratio between the current in the strand with the peak power dissipation and the average strand current at the instant of quench.

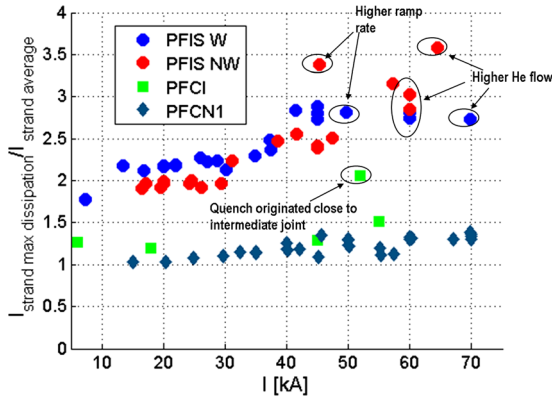

FIG. 19. Overload of the strand with peak power dissipation at quench versus quench current.

Although they remain stable around 2.2 and 2.0 for PFIS W and PFIS NW, respectively, up to 30 kA, the strand overloads increase for higher quench currents which leads in the end to premature quenches. The increase of the unbalance in this sample was already indirectly foreseen in Ref. 5 on the ground of the growing difference between experimental quench current and peak field critical current estimation. Since the threshold for the overload rise does not coincide with the quench regime transitions previously identified, no clear quantitative correlation could be determined between strand overload and premature quench of the conductor at present. Therefore, the analysis suggests that no comprehensive conclusions can be drawn focusing exclusively on the current unbalance, but other factors may need to be taken into account.

Regarding the PFCI, Fig. 19 shows that the strand overload at quench is much lower (~1.3–1.4) and hardly varies with quench current. Since the coil featured the same strand, cable, and joint design as the PFIS, the improvement of the current unbalance is related to the higher distance between joints and high field region, allowing for a better redistribution of the non-uniformity.

For only one point in the PFCI data, at 52 kA, the strand overload is found to be comparable to the values of PFIS. However, the result of this particular run has been incorrectly localised in the cable. Although the measurements show that the quench originates in the middle of the main winding, JackPot predicts the quench to start close to the intermediate joint. A more detailed knowledge of the temperature profile along the coil would be essential for improving the definition of the quench origin in the simulation, but it is not available.

TABLE III. Peak quench power and current non-uniformity of the samples at operating conditions of ITER PF coils.

	PFIS W	PFIS NW	PFCI	PFCN1
Type	PF1	PF1	PF1	PF2
Nominal operating current [kA]	52.0	52.0	52.0	50.0
Nominal effective peak field [T]	5.7	5.7	5.7	5.0
Strand peak power at quench [mW/cm^3]	0.02	800	640	65
Cable power at quench [mW/cm^3]	8×10^{-7}	0.4	0.15	0.21
Current non-uniformity at quench	3.05	2.8	1.45	1.25

The final sample (PFCN1) shows the lowest and most stable current unbalance of all the analyzed conductors. Since the PFCN1 is a short sample like the PFIS, no significant current re-distribution is expected between joint and high field region due to the short intermediate distance. The improved current uniformity, therefore, comes from the new layout employed for the upper terminations and from the exclusion of the bottom joint.

Table III provides a summary of the peak power at quench and current non-uniformity level at operating conditions for the analyzed samples.

As already observed, the simulation results show that the PFIS cables could reach higher local peak powers than the PFCN1 and, to a less extent, than the PFCI. Although speculative and not supported by the analysis presented here, the most likely explanation is that the local higher peak power in the PFIS could be explained by a larger temperature gradient and thus better cooling of the hot spots by their immediate surroundings. In the case of large current non-uniformity, the heat in the cable volume is concentrated in very small spots with much higher temperature than most of the surrounding strand volume characterized by a much lower dissipation. This surrounding cable volume at lower temperature offers better cooling conditions than in cables with more homogeneously distributed power dissipation. This possible thermal phenomenon cannot be clearly separated from the so-called cable and strand quench regimes as observed for the PFIS. In addition, it should be remarked that the PFCN1 cable is made of different strands, and the cable has a different configuration.

IX. EFFECT OF JOINT AND SAMPLE LAYOUT

The current non-uniformity between the strands originating at the joints is in itself unavoidable because of the natural spread in the strand to joint contact resistances. However, the analysis points out a number of factors that can help reducing such an unbalance.

The best balanced current distribution was achieved for the PFCN1 through the elimination of the bottom joint and the individual soldering of the petals at the upper terminations. The effect of the latter solution is to increase the number of strands directly in touch with the termination block. Alternative ways to achieve this result could be increasing the joint length, decreasing the last cabling stage twist pitch or increasing the Cu sole-CICC contact surface. However, the possibility of higher coupling losses during AC operation may restrict the effectiveness of these solutions.

Apart from reducing the current unbalance at its source, i.e., strand to joint contacts, another solution may be to facilitate its redistribution along the conductor. In this respect from the analysis, the main driving force appears to be a magnetic (and eventually thermal) gradient along and in the cross section of the CICC. However, current redistribution generally requires significant lengths (several meters) of conductor, which makes it an ineffective cure to the problem in the case of short samples. Moreover, the length of the sample

may not be enough for "safe" operation even in the case of long coils when joints are placed in relatively high field regions. This is demonstrated by the Intermediate Joint of the PFCI. In this case, the presence of a second cooling circuit slightly lowering the joint temperature proved to be crucial in preventing the consequences of elevated power dissipation close to the joint coming from high current unbalance and magnetic field.

The removal of wraps in the joints was observed to cause a small reduction of the current unbalance in the two legs of the PFIS, but it was not sufficient to avoid the risk of premature quenches. Solder can be used to reduce the electrical resistance between strand and copper sole in the joints and improving redistribution. However, its effect clearly depends on the thickness of the solder layer. Both these solutions will increase the AC losses and further work is needed to determine the optimum compromise between DC resistance and AC power loss.

Finally, the cabling pattern may also influence the current distribution in a CICC. However, it is not possible to assess the impact of this factor on the base of the available data since the two samples with different cable layouts (PFIS and PFCN1) had also other major variations regarding the join/termination design as well as strand properties.

X. CONCLUSIONS

Using the code JackPot, we have quantitatively determined the influence of the sample and joint layout on the current distribution and its relation with strand and cable power dissipation at quench for both ITER PF short samples and coils. The importance of this analysis lays in quantitatively specifying the boundaries for the design of the ITER PF coils within the coil-joint configuration, joint properties, and applied magnetic field conditions. The strand power dissipation at quench sets a clear limit to the allowed current non-uniformity. In turn, this determines the joint properties in the sense of resistivity of the used components, which are chosen to limit heat dissipation originated by AC losses from magnetic field variations.

Although lacking of a thermal-hydraulic description of the CICC, the model computes the instantaneous power dissipated in the strands, once the quench conditions are known from the experiment. JackPot allowed the determination of the T_{cs} of the analysed samples in all experimental conditions with a maximum error of 0.12 K thanks to the detailed level of joint and strand current modelling. The result is up to now a great improvement in accuracy compared to other existing codes. Moreover, for the first time, the detailed power dissipation distribution and current non-uniformity of the analysed samples could be quantified and visualized.

According to the model, a quench in large NbTi CICCs is initiated in relatively small isolated hot spots often composed by single wires with peak dissipation along lengths of less than 1 cm. The hot spots are located in the high magnetic self field zone of the cable cross section. In case of elevated current non-uniformity among the strands, the peak power dissipation increases with cable current.

For the PFIS, the cable and strand peak power dissipations drop at the same current levels at which sudden quenches start being observed in the experiments. The behaviour is explained in terms of different quench regimes: at low currents, the quench is determined by the global cable behaviour, whereas at high currents, localized power dissipation on single strand level is responsible for the quench. The strand quench regime transition is not observed for PFCI and PFCN1. Both samples show reduced strand peak power densities at quench due to more homogeneous current distribution. The improved current distributions in the latter two samples are caused by either longer distance between the joints and the high field region (PFCI), or an improved joint design (PFCN1). No clear quantitative correlation could be verified between the current unbalance of PFIS and the quench regime transition. Despite this, the constantly increasing strand current overload can be regarded as the origin of the observed premature quenches.

From the simulation results, a maximum current unbalance of 1.45 at operating conditions is allowed in ITER PF cables to avoid the transition to the quench strand regime and prevent the risk of sudden quenches. In these conditions, the expected cable power dissipation at quench is in the range of 0.15–0.25 mW/cm^3. The strand peak power varies, depending on the strand characteristics and cable configuration, between 65 and 640 mW/cm^3.

The initial assumption that by first order approximation the small scale and local electrical-thermal strand interactions were not required for a pragmatic performance analysis appears justified. The influence of these effects is identified as being marginal and far less than the generally accepted temperature margin for safe operation of large sized NbTi CICCs. This means that the approach is allowed to be used for joint design and setting the safety limits for peak power dissipation and maximum current non-uniformity.

APPENDIX: DETAILS OF THE ANALYSED SAMPLES AND CONDUCTORS

Tables IV–VI summarise the main characteristics of the analysed conductors, such as strand and cable diameters, cabling sequence, and twist pitches.

TABLE IV. PFIS conductor and sample parameters.

	PFIS W	PFIS NW
Number of SC strands	1440	
Strand diameter [mm]	0.73	
Cabling sequence	$3 \times 4 \times 4 \times 5 \times 6$	
Last stage twist pitch [mm]	489	530
Cable outer diameter [mm]	38	
	Bottom joint	Upper termination
Termination length [mm]	450	420
Cu plate RRR	41	86
CuCrZr sleeve RRR	2.5	
Sleeve–plate contact angle	135°	
Sleeve outer diameter [mm]	42	
Strand-sleeve soldering	Ag coating + sleeve tinning	

TABLE V. PFCI conductor and sample parameters.

	PFCI
Twist pitch sequence [mm]	$45 \times 85 \times 125 \times 160 \times 410$
Cu plate RRR	300
CuCrZr sleeve RRR	6
Strand-sleeve soldering	SnPb paste coating

TABLE VI. PFCN1 conductor parameters.

	PFCN1
Number of SC strands	720
SC strand diameter [mm]	0.76
Cabling sequence	((((2 SC + 1 Cu strand) × 3 × 4 + 1 Cu core 1) × 5) + 1 Cu core 2) × 6
Twist pitches [mm]	$45 \times 85 \times 145 \times 250 \times 450$
Cable outer diameter [mm]	35.3

For the PFIS and PFCI samples, details are also provided about the differences existing between their terminations and joints. Although sharing the same layout, the terminations and joints of the PFCI featured improved material properties and strand-to-sole soldering procedure. These changes were required due to the excessively high termination/joint resistance measured for the PFIS sample, which exceeded the ITER acceptance criteria.

[1]P. Bruzzone, M. Bagnasco, D. Bessette, D. Ciazynski, A. Formisano, P. Gislon, F. Hurd, Y. Ilyin, R. Martone, N. Martovetsky, L. Muzzi, A. Nijhuis, H. Rajainmäki, C. Sborchia, B. Stepanov, L. Verdini, R. Wesche, L. Zani, R. Zanino, and E. Zapretilina, IEEE Trans. Appl. Supercond. **15**, 1351 (2005).
[2]Y. A. Ilyin, A. Nijhuis, H. H. J. ten Kate, P. Bruzzone, and B. Stepanov, IEEE Trans. Appl. Supercond. **15**, 1391 (2005).
[3]Y. Ilyin, A. Nijhuis, and H. H. J. ten Kate, Cryogenics **46**, 517 (2006).
[4]A. Nijhuis, Y. Ilyin, and H. H. J. ten Kate, IEEE Trans. Appl. Supercond. **16**, 868 (2006).
[5]R. Wesche, B. Stepanov, and P. Bruzzone, IEEE Trans. Appl. Supercond. **16**, 819 (2006).
[6]R. Zanino, M. Bagnasco, D. Ciazynski, B. Lacroix, E. P. A. van Lanen, S. Nicollet, L. Savoldi Richard, C. Sborchia, A. Torre, A. Vostner, and L. Zani, Supercond. Sci. Technol. **22**, 085006 (2009).
[7]F. H. Hurd, C. Sborchia, E. Salpietro, D. Duglue, C. Keefe, S. Bates, P. Pesenti, A. della Corte, P. L. Bruzzone, and M. Polak, IEEE Trans. Appl. Supercond. **15**, 1379 (2005).
[8]F. H. Hurd, H. Rajainmäki, E. Salpietro, C. Sborchia, P. Bruzzone, and C. Keefe, "Status of investigations on PF conductor insert (PFCI) joints," in 5th Meeting of PFIS Testing Group, PSI Villigen, 2004.
[9]C. Sborchia, D. Duglue, F. Hurd, R. Maix, E. Salpietro, P. Testoni, D. Bessette, N. Mitchell, K. Okuno, M. Sugimoto, A. Alekseev, and V. Sytnikov, Fusion Eng. Des. **66–68**, 1081 (2003).
[10]W. Baker, C. Keefe, H. Rajainmäki, and E. Salpietro, Fusion Eng. Des. **82**, 1567 (2007).
[11]H. Rajainmäki, private communication (2010).
[12]B. Liu, Y. Wu, F. Long, and S. Li, Cryogenics **51**, 90 (2011).
[13]L. Reccia, "ENEA report on ITER contract," Report No. CT/09/4300000048 (2010).
[14]L. Muzzi, G. De Marzi, C. F. Zignani, U. B. Vetrella, V. Corato, A. Rufoloni, and A. della Corte, IEEE Trans. Appl. Supercond. **21**, 3132 (2011).
[15]L. Bottura, IEEE Trans. Appl. Supercond. **10**, 1054 (2000).
[16]E. P. A. van Lanen and A. Nijhuis, Cryogenics **50**, 139 (2010).
[17]E. P. A. van Lanen, and A. Nijhuis, Cryogenics **84**, 1912 (2009).
[18]Y. A. Ilyin, A. Nijhuis, W. Abbas, P. Bruzzone, B. Stepanov, L. Muzzi, P. Gislon, and L. Zani, IEEE Trans. Appl. Supercond. **15**, 1359 (2005).
[19]F. Cau, M. Bagnasco, P. Bruzzone, M. Calvi, and F. Roth, IEEE Trans. Appl. Supercond. **19**, 1452 (2009).
[20]E. P. A. van Lanen, L. Feng, R. P. Pompe van Meerdervoort, W. A. J. Wessel, and A. Nijhuis, IEEE Trans. Appl. Supercond. **20**, 474 (2010).
[21]R. Zanino, M. Astrov, M. Bagnasco, W. Baker, F. Bellina, D. Ciazynski, S. Egorov, K. Kim, J. L. Kvitkovic, B. Lacroix, N. Martovetsky, N. Mitchell, L. Muzzi, Y. Nunoya, K. Okuno, M. Polak, P. L. Ribani, E. Salpietro, L. Savoldi Richard, C. Sborchia, Y. Takahashi, P. Weng, R. Wesche, L. Zani, and E. Zapretilina, IEEE Trans. Appl. Supercond. **17**, 1353 (2007).
[22]D. Ciazynski, D. Bessette, P. Bruzzone, N. Martovetsky, B. Stepanov, R. Wesche, L. Zani, R. Zanino, and E. Zapretilina, IEEE Trans. Appl. Supercond. **15**, 1355 (2005).
[23]R. Zanino, F. Bellina, P. L. Ribani, and L. Savoldi Richard, Supercond. Sci. Technol. **24**, 105001 (2011).
[24]G. Willering, Ph.D. dissertation (University of Twente, 2009).
[25]N. Amemiya, H. Yonekawa, E. Kobayashi, T. Ogitsu, K. Sasaki, N. Ohuchi, K. Tsuchiya, and T. Shintomi, Cryogenics **43**, 249 (2003).
[26]G. Bansal, K. Seo, N. Yanagi, T. Hemmi, K. Takahata, T. Mito, B. Sarkar, and Y. C. Saxena, IEEE Trans. Appl. Supercond. **18**, 1245 (2008).